applied sciences

MDPI

Article

Microstructured Phononic Crystal Isolates from Ultrasonic Mechanical Vibrations

Valentina Zega [1], Luca Pertoldi [2], Tommaso Zandrini [2], Roberto Osellame [2], Claudia Comi [1,*] and Alberto Corigliano [1]

[1] Dipartimento di Ingegneria Civile e Ambientale, Politecnico di Milano, Piazza Leonardo da Vinci, 32-20133 Milano, Italy; valentina.zega@polimi.it (V.Z.); alberto.corigliano@polimi.it (A.C.)
[2] Istituto di Fotonica e Nanotecnologie (IFN), Consiglio Nazionale delle Ricerche (CNR), Piazza Leonardo da Vinci, 32-20133 Milano, Italy; luca.pertoldi@polimi.it (L.P.); tommaso.zandrini@polimi.it (T.Z.); roberto.osellame@polimi.it (R.O.)
* Correspondence: claudia.comi@polimi.it; Tel.: +39-0223994215

Abstract: The functioning of many micro-electromechanical devices with parts oscillating at high frequencies require isolation from external vibration. Phononic crystals, presenting band-gaps in the dispersion spectrum, i.e., interval of frequency in which propagating waves are attenuated, can provide an effective solution for vibration shielding at the microscale. In the present work, we design—through numerical simulations—a 3D phononic crystal with a micrometric unit cell able to work as vibration isolator for a micro system. We exploit the direct writing technique based on two-photon polymerization to realize three prototypes of different dimensions. Experimental measurements performed with a Michelson interferometer demonstrate the effectiveness of the proposal.

Keywords: metamaterial; two-photon polymerization; band gaps

Citation: Zega, V.; Pertoldi, L.; Zandrini, T.; Osellame, R.; Comi, C.; Corigliano, A. Microstructured Phononic Crystal Isolates from Ultrasonic Mechanical Vibrations. *Appl. Sci.* **2022**, *12*, 2499. https://doi.org/10.3390/app12052499

Academic Editor: Dimitrios Zografopoulos

Received: 4 February 2022
Accepted: 25 February 2022
Published: 27 February 2022

1. Introduction

Micro electro-mechanical systems (MEMS) [1] are now ubiquitous in portable electronic devices, automotive and industrial applications, where they act as integrated sensors and actuators. These components are fundamental in defining the 'smartness' of the equipment and play a key role in fast-developing fields like IOT, industry 4.0, autonomous cars, advanced structural health monitoring and collaborative robots. The potentialities of micro (and nano) sensors and actuators are often limited by standard fabrication technologies strictly related to planar lithographic techniques. The lack of true three-dimensional fabrication processes in MEMS has prevented, so far, the development of devices in which fully 3D micro-structures can enhance sensitivity and actuation performances or the exploitation of new physical principles to govern signals [2–5].

Three-dimensional metamaterials inserted in MEMS design could pave the way to a new paradigm of MEMS. Micro-devices with the ability to completely control the transmission of elasto-acoustic waves in three directions, in ranges of frequencies spanning hundreds of kHz to some MHz, could, e.g., be obtained by exploiting the performances of 3D phononic crystals (see, e.g., [6–8] and the recent review papers [9–11]).

MEMS operation is often based on micro-scale movable parts oscillating at specific resonance frequencies [12,13] that are affected by external vibrations that introduce undesired noise and can even compromise the right functioning [14,15]. Isolation of MEMS from such external vibrations is essential for their correct functioning [16–18]. A typical example is that of MEMS resonators used for clock applications [19–21] which must permanently oscillate at specific frequencies, in the order of hundreds of kHz or a few MHz. Complete protection from external vibration in specific frequency ranges is, therefore, of paramount importance. This can be offered with unparalleled performances by introducing into the MEMS design an isolation layer based on 3D phononic crystals endowed with ultra-wide

complete band gaps [22–26], whose properties do not rely exclusively on the intrinsic material properties, but mainly on their fine-scale structuring. Complete isolation, instead of vibration damping, can be obtained with attenuation factors that are orders of magnitude higher than those obtainable with a bulk material.

The increasing interest on applications of phononic crystals in different contexts is testified by several recent works focused on the design and optimization of phononic crystals in terms of bandgap width, or on the miniaturization of such structures. Examples of topological optimization of phononic crystals [27], e.g., by using the SIMP approach and the MMA algorithm [28], genetic algorithms [29], the bidirectional evolutionary structural optimization (BESO) [30,31] or the gradient-based approach [32], are indeed available. In parallel, examples of miniaturized phononic crystals are present in the recent literature [33–36].

In this work, we take a step further with respect to the available literature by combining the ultra-wide bandgap property of an optimized phononic crystal with the very small dimensions, i.e., in the order of µm, required by the MEMS world, thus opening the path to the possibility to integrate MEMS with metamaterials for vibration isolation purposes.

The proposed prototype is studied, fabricated and tested to demonstrate its isolation properties. It is shown that attenuation factors of several orders of magnitude are obtained. The 2PP technique, exploiting the nonlinearity of the absorption process and setting the intensity just above the threshold, can overcome the diffraction limit, obtaining resolutions down to hundreds of nanometres using a laser beam with wavelength of several hundreds of nanometers [37–39]. 2PP-based manufacturing processes share with other additive manufacturing (AM) techniques, such as stereolithography, selective laser sintering, 3D printing, electron beam melting, and direct metal laser sintering, the ability to realize microarchitected materials with unlimited topological complexity, while increasing the resolution to the microscale [10,40]. The limitations of the 2PP technique are mainly related to the choice of building material. However, even though the resin usually employed has a relatively low elastic stiffness, the small dimensions of the microstructure that can be fabricated allow us to obtain phononic crystals with isolation properties in the range of interest to the MEMS applications targeted here (from hundreds of kHz to some MHz).

The isolation properties of the proposed and fabricated phononic microstructures are then experimentally verified. The role of the stratification induced by the technique of two-photon polymerization is finally studied.

2. Design of 3D Phononic Crystals

The design of the unit cell of the phononic crystal proposed in this paper is inspired by the work recently published by co-authors [41]. The phononic crystal proposed in [41] is indeed very promising for our target applications since it exhibits an ultra-wide bandgap, i.e., gap to mid-gap ratio of 132% and is fully compatible with the 2PP fabrication technique we want to employ.

In [41], the design was obtained as a three-dimensional generalization of the two-dimensional phononic crystals proposed and optimized in terms of the gap to mid-gap ratio in [30]. The 2D unit cell topology chosen was made by an external frame with half circles centred in the middle-point of the edges, the bidirectional evolutionary structural optimization (BESO) gave the optimal frame thickness and radius of the circles. In particular, the high mass of the circles and low frame thickness and stiffness allow to separate the global and local modes resulting in a wide band-gap.

In the 3D extension proposed in [41], the symmetries and proportions of the optimal 2D geometry are preserved, ending up with a cubic structure where each face has the planar topology of the 2D counterpart. Again, the high mass of the spheres and low stiffness of the connecting beams allow for a large band-gap formation.

In the present work, a slightly different geometry is proposed, with masses that are no more semi-spherical and with modified relative dimensions between the masses and the beams connecting the masses. The new unit cell is reported in Figure 1a: it consists of six masses obtained by cutting a semi-sphere through a plane parallel to the

sphere section, connected through three straight beams of length $0.44a$ and a square cross section of dimension $0.075a$, with a being the dimension of the unit cell along the three orthogonal directions.

Thanks to the cubic symmetry of the unit cell, the dispersion diagram can be computed by chosing the tetrahedron drawn in Figure 1b as the irreducible Brillouin zone (IBZ). The phononic band structure can be obtained by imposing Floquet periodic boundary conditions on the six sphere sections of the unit cell and performing a parametric sweep over the wave vector according to the Bloch theorem [42]:

$$u_j(x+a, y+a, z+a) = u_j(x, y, z)e^{i(k_x a + k_y a + k_z a)} \quad (1)$$

where u_j denotes the elastic displacement vector along the x-, y- and z-directions and k_x, k_y and k_z are the components of the Bloch wave vector. In a finite element method (FEM) code, Floquet boundary conditions can be implemented, as explained, e.g., in [43]. To compute the dispersion diagram, the 3D geometry of the unit cell is then discretized through 30,000 quadratic tetrahedral elements to guarantee at least four elements in the beams thickness and a consequently good accuracy of the results. The numerical phononic band structure is finally computed by means of the solid mechanics module of COMSOL Multiphysics v5.6, and it is shown in Figure 1b in a non-dimensional form. The non-dimensional frequency f_{nd} is defined as the product of the dimensional frequency f with the ratio a/v, with $v = \sqrt{E/\rho}$ being the sound velocity of the material (E and ρ are the Young's modulus and the mass density of the bulk material). The first full 3D bandgap is characterized by a gap to mid-gap ratio of 134.87%, with non-dimensional frequency limits equal to 0.113 and 0.581. According to the Bragg-based bandgap formation mechanism, as the cell dimension a decreases, the actual, dimensional, frequency of the band-gap increases. An increase in the Young's modulus E of the bulk material also results in a shift of the bandgap towards higher frequencies. The ultra-wide bandgap exhibited by the proposed phononic crystal is justified by the modal shapes of the bandgap opening and closing modes. As clearly visible from Figure 1b, the opening mode involves masses and beams, while the closing mode is local and only related to beam deformations; thus, resulting in a significant difference in terms of natural frequency and in an ultra-wide bandgap.

To verify the claimed attenuation properties in a finite prototype made by $2 \times 2 \times 3$ unit cells and fabricated through the 2PP technique, a non-dimensional transmission diagram was also numerically computed in COMSOL Multiphysics v5.6. The $2 \times 2 \times 3$ configuration was chosen as a compromise between attenuation efficiency, which increases with the number of cells and compactness of the overall structure. A glass support and a top plate ($2a \times 2a \times 14$ µm) of the same material of the phononic crystal were also considered in the analysis to simulate the experimental set-up employed in the following. The 3D geometry was discretized through 224,000 quadratic tetrahedral elements. Free boundary conditions were applied on all the lateral surfaces of the phononic crystal and on the surface of the top plate, while a prescribed frequency-dependent z-axis displacement was assigned at the bottom surface of the glass support, as shown in Figure 1c. A frequency domain analysis was then performed in the range of frequency 0 MHz–8 MHz with a step of 400 Hz. The output was computed for each forcing frequency as the average z-axis displacement experienced by the upper surface of the top plate, as shown by the black arrow in Figure 1c. The non-dimensional transmission diagram is reported in Figure 1c, it shows a good agreement with the dispersion plot reported in Figure 1b. Three peaks are present in the attenuation dip of the transmission diagram. They correspond to global modes of the top plate, as shown in the inset of Figure 1c and do not compromise the correct functioning of the metastructure, as expected.

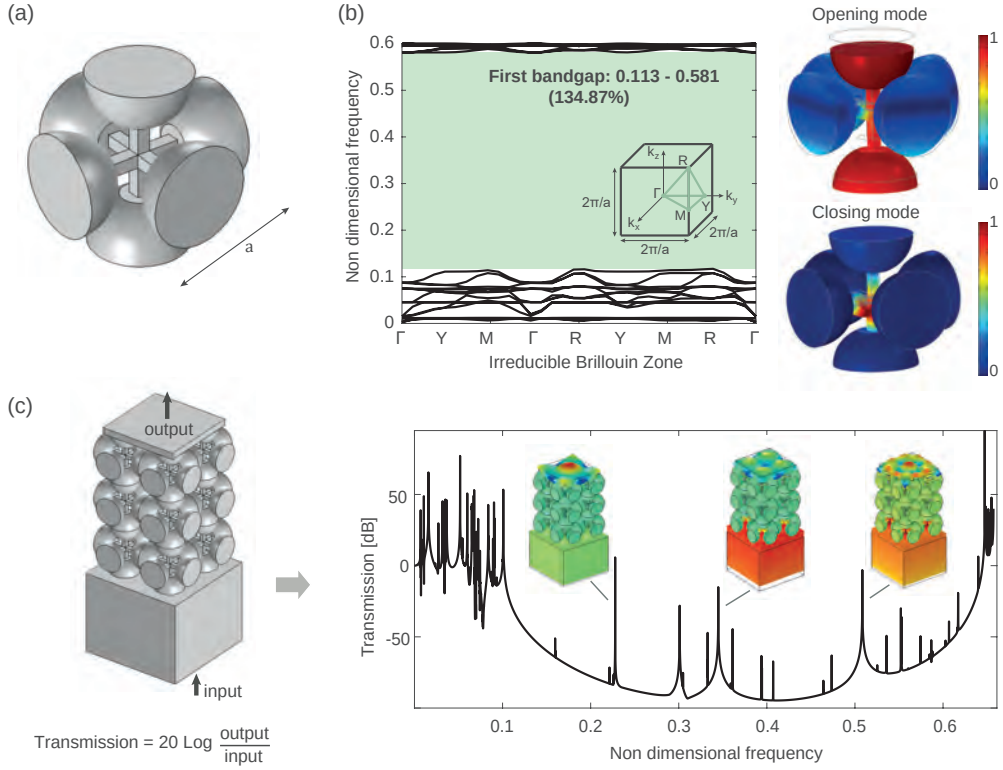

Figure 1. (**a**) Unit cell of the proposed phononic crystal, with a the dimension of the cubic cell. (**b**) Non-dimensional dispersion diagram with non-dimensional frequency $f_{nd} = fa/v$. The irreducible Brillouin zone (IBZ) and the bandgap opening and closing modes are also reported. (**c**) Non-dimensional transmission diagram computed on a $2 \times 2 \times 3$ phononic crystal. The input is prescribed as a z-axis displacement at the bottom surface of the glass support, while the output is measured as the average z-axis displacement of the top plate (black arrows).

3. Fabrication and Characterization of the Phononic Crystal

3.1. Material and Writing Procedure

To fabricate the phononic crystal described in Section 2, with typical cell dimensions spanning from 100 µm to 200 µm, we used the two-photon polymerization technique. In particular, the hybrid organic/inorganic negative photoresist SZ2080 was employed in this work for its good optical and mechanical properties and its good dimensional stability with negligible shrinkage.

The set-up for the fabrication includes a femtosecond laser source (Toptica, FemtoFiber pro NIR) operating at its second harmonic and emitting mode-locked pulses at 780 nm wavelength. This source has a repetition rate of 80 MHz and a pulse length of about 80 fs. To generate the 3D photopolymerized structures, the beam scans the resin that has been previously dropcasted on a glass substrate in a layer-by-layer pattern. In particular, movements in the x-y plane were achieved with XY linear stages (ANT95-50-XY, Aerotech), while movements along the z-axis were performed using a linear stage (ANT130-035-L-ZS, Aerotech) that translates the 40× objective lens (Carl Zeiss, N-Achroplan 40× WI and 0.75 NA). Beam passage control was obtained with a fast galvanometric shutter, while beam intensity control was achieved with a polarizer and a waveplate. After the photopolymerization process, the samples were developed in a solvent to remove the unpolymerized resin.

As shown in [44,45], the mechanical properties (in particular the Young's modulus) of the two-photon polymerized SZ2080 strongly depend on the different writing parameters: power of the laser, writing speed, distance between lines. Moreover, differently from [44], we here employ a water-immersion objective lens 40× to speed-up the fabrication process, thus obtaining a polymerized SZ2080 with different stiffness with respect to [44].

3.2. Experimental Set-Up

To measure the attenuation properties of the metastructures, a Michelson interferometer is here employed. The set-up is shown in Figure 2. The microstructure is fixed on its basis and excited by a piezoelectric disk. The laser beam is split into two rays, which reflect separately on a mirror and on the structure, respectively. When the structure oscillates in the vertical direction, the reflected rays combine and interfere. The interference spot is detected by the photodiode and from the oscilloscope one can register a modulated signal.

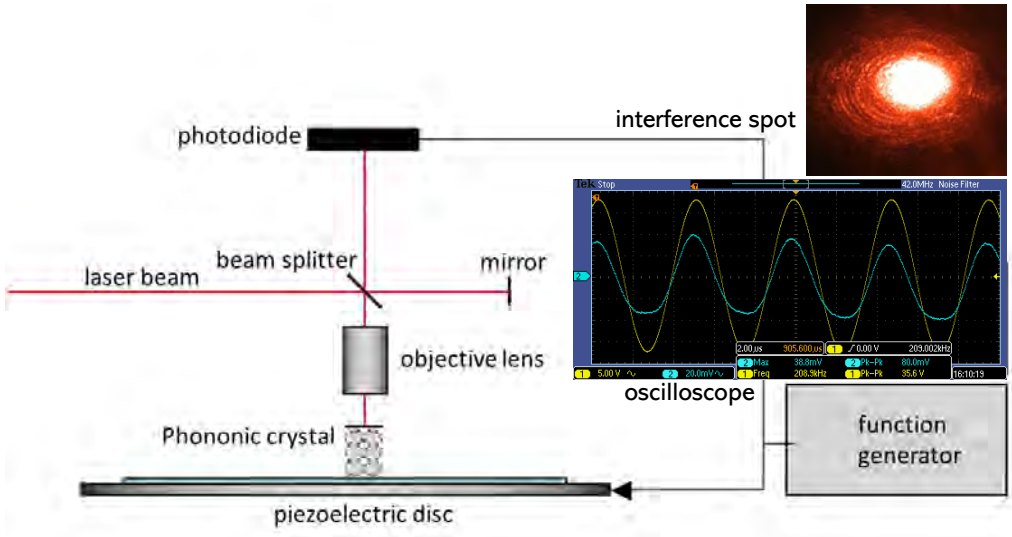

Figure 2. Michelson interferometer used to perform experimental tests on the three fabricated structures.

4. Results

4.1. Phononic Microstructures

Several micro-phononic crystals made by 2 × 2 × 3 unit cells have been fabricated. Three different cell dimensions *a* have been selected: 100 µm, 150 µm and 200 µm, the obtained structures are shown in Figure 3 where the unit cells are highlighted. From these scanning electron microscope images one can see that the 2PP fabrication technique is suitable to realize the very complex 3D geometry of the metamaterial at the microscale.

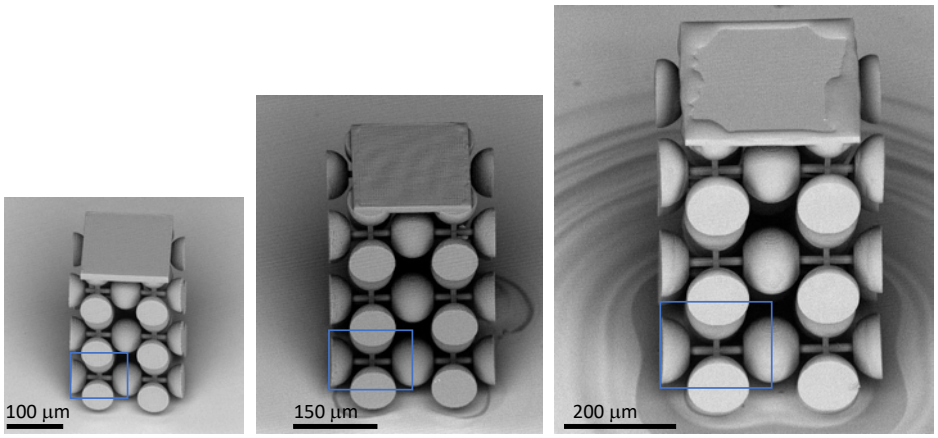

Figure 3. Scanning electron microscope images of the fabricated micro-phononic structures with unit cells of 100 µm, 150 µm and 200 µm.

The final dimensions of the three fabricated structures slightly differ from the ideal geometry described in Section 2, due to fabrication process constraints. In particular, the ellipsoidal shape of the voxel, which, in the present fabrication, has in-plane axes of 2 µm

and out-of-plane axis of 6 µm, leads to a 10% increase of the unit cell height, thus resulting in overall dimensions of 100 × 100 × 110 µm^3, 150 × 150 × 165 µm^3 and 200 × 200 × 220 µm^3. On the other hand, the development phase of the resin leads to slightly different dimensions of the cross section of the beam elements with respect to the nominal ones. Finally, some corrections on the geometrical dimensions of the beam elements are applied by design to guarantee the fabricability, especially for the smaller structures considered here. Table 1 reports the actual dimensions of the unit cell beam elements measured with scanning electron microscope after fabrication.

Table 1. Geometrical parameters of the fabricated structures.

Cell Size *a*	Beam Squared Cross Section	Beam Length (*x*-/*y*-Axis)	Beam Length (*z*-Axis)
100 µm	7.5 µm	44 µm	48 µm
150 µm	10 µm	70 µm	76 µm
200 µm	12 µm	98 µm	106 µm

4.2. Oscillation Measurements

A piezoelectric disk, a PRYY+0189 by PICeramics with resonant frequency of 2 MHz (thickness: 1 mm and diameter: 25 mm), is here employed to excite the three fabricated microstructures. Before proceeding with the experimental tests on the metastructures, we first characterized the piezoelectric disk . The disk is inserted in a circuit, excited at different frequencies and the voltage drop is recorded. The dynamic response is shown in Figure 4a.

A finite element analysis of the disk showed that the drops in the voltage correspond to eigenfrequencies of the radial modes, represented in Figure 4b. Although radial, these resonant modes have a strong effect on the vertical oscillation. This is confirmed by the measurements obtained by the Michelson interferometer directly on the glass, without metastructure, where the eigenfrequencies of the disk are clearly visible, see Figure 4c.

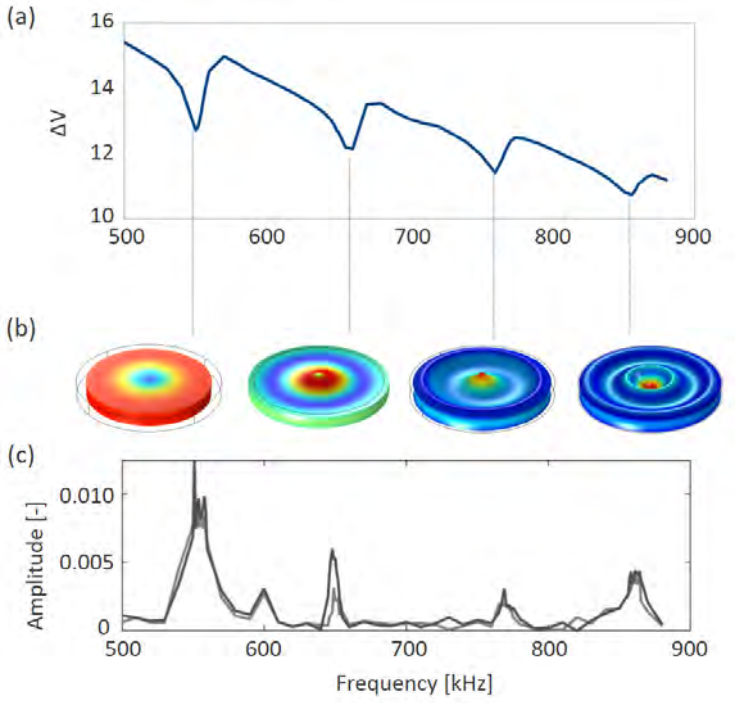

Figure 4. (**a**) Piezoelectric actuator signal: variation of potential versus frequency. (**b**) Radial modes of the piezoelectric disk. (**c**) Photodiode signal on glass.

Figure 5 shows the measurements obtained with the three metastructures of different dimensions. Two metastructures with unit cell dimension of 100 µm are tested to double

check the employed set-up. As expected, the smallest metastructure only attenuates the peak due to resonance of the actuator at the highest frequency (870 kHz); with the unit cell of 150 µm and the intermediate peak (780 kHz) is attenuated, while with 200 µm three peaks are attenuated. These results show the selective vibration isolation properties of the metastructures and indicate that the actual opening frequency of the band-gap of the three crystals falls inside the shaded regions in Figure 5.

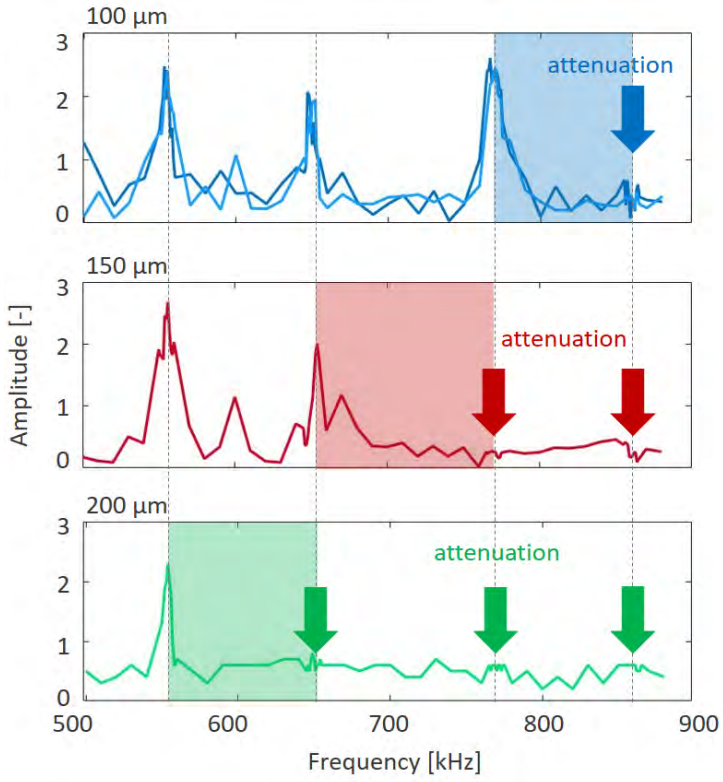

Figure 5. Signal transmitted by the micro-phononic structures at varying frequency for the 100 µm, 150 µm and 200 µm unit cell dimension.

5. Discussion

Dispersion and transmission analyses exploited in the design phase and described in Section 2 have been repeated on the actual geometries of the three microstructures of Figure 3 to compute the expected attenuation properties. For the supporting glass the elastic modulus $E = 72$ GPa, the Poisson's coefficient $\nu = 0.23$ and the mass density $\rho = 2500$ Kg/m^3 have been employed, while for the resin, typical parameters ($E = 2.3$ GPa, $\nu = 0.42$ and $\rho = 1200$ Kg/m^3) available in the literature [45] were assumed.

In Figure 6, transmission diagrams computed for the three fabricated metastructures are reported. Bandgaps estimated through dispersion analyses under the hypothesis of infinite periodic structure are also reported as shaded areas. The small discrepancies can be ascribed to the finite dimension of the fabricated metastructures, to the presence of the supporting glass and of the top plate. Note that the apparent interruption of the bandgap shown for the unit cell dimension of 100 µm and 200 µm is only due to flat modes (as described in, e.g., [46,47]) that do not compromise the correct functioning of the metastructure and that will be neglected in the following.

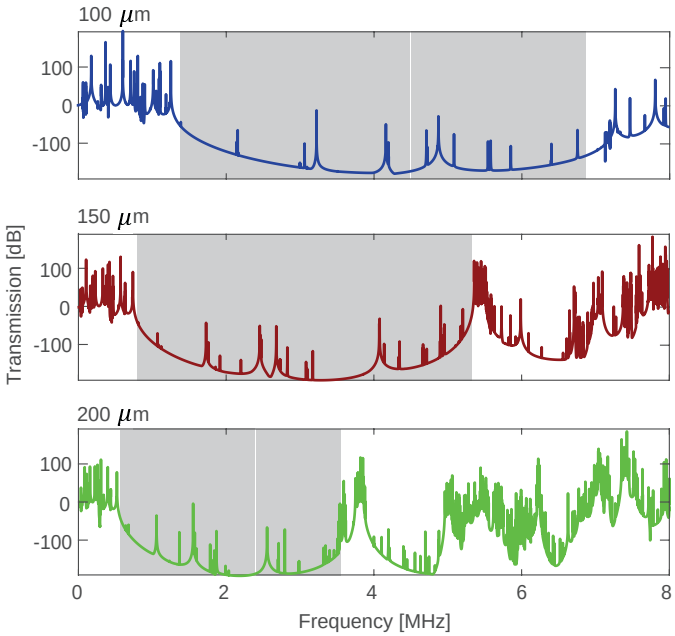

Figure 6. Transmission diagrams numerically computed for the three fabricated metastructures. Bandgaps estimated through dispersion analyses are reported as shaded grey areas.

Comparing numerical predictions of Figure 6 with measurements reported in Figure 5, one can observe a qualitative agreement for the three fabricated structures. The quantitative agreement is instead obtained only for the bigger structure ($a = 200$ µm).

To explain this behavior several aspects should be considered.

Firstly, it is worth mentioning that the 2PP technique fabricates layered structures in the printing direction, i.e., z-axis, with the number of overlapping layers determined by the voxel dimension and by the chosen spacing in the printing direction, as explained in [44]. For the fabrication process employed in this work, the z-axis voxel dimension was about 6 µm, while the z-axis slicing was 1 µm. To evaluate the influence of this layered structure, we supposed that the bulk mechanical properties of the resin was obtained through at least three superimposed layers and that, as an example, a 25% and 50% reduction in the Young's modulus was obtained in the presence of two superimposed layers and just one layer, respectively. Horizontal beams inside the unit cell must hence be considered layered, as reported in Figure 7a. Each beam was divided into three regions where, (i) one superimposed layer (orange), (ii) two superimposed layers (green) and (iii) at least three superimposed layers (grey) were present. By considering a Young's Modulus equal to 2.3 GPa in the central area, to 1.725 GPa in the *two-layers* area (1 µm) and to 1.15 GPa in the *one-layer* area (1 µm) according to our assumption and running again dispersion analyses in COMSOL Multiphysics for the three unit cells, the original bandgaps (reported as grey bars in Figure 7b) shifted towards smaller frequencies (orange bars in Figure 7b). The influence of the stratigraphy was different for the three cells and higher for the smaller ones, with the voxel dimension being the same and the beam thickness different (Table 1). Due to the uncertainties on the mechanical properties of each layer and to the number of superimposed layers needed to obtain fully developed material properties, it is not possible to make a quantitative estimation. However, on the basis of the test case shown here, we can state that layers play an important role in terms of reduction of the opening frequency at the fixed bulk Young's modulus, especially for smaller structures.

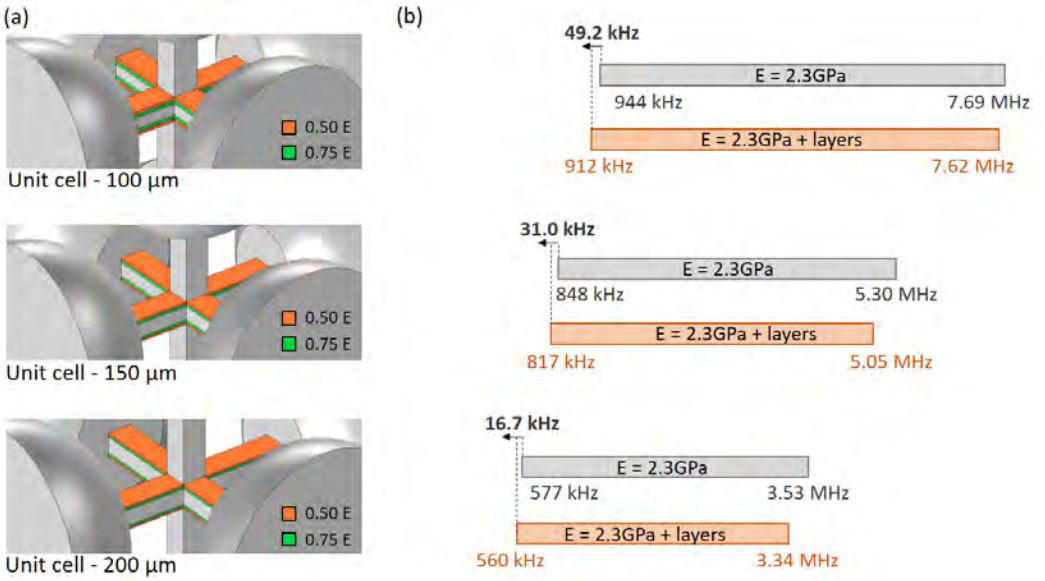

Figure 7. (**a**) Close-up view of the unit cell beams for a = 100, 150, 200 µm. The layered structure caused by the 2PP fabrication process is put in evidence: *one*, *two*, *at least three* overlapped layers areas are shown in orange, green and grey, respectively. (**b**) Bandgap simulated through dispersion analyses under the hypothesis of uniform Young's Modulus (grey bars) and layered structure (orange bars). The reference Young's modulus of 2.3 GPa was adopted for the uniform structure and for the *at least three* overlapped layers area, while reduced Young's modula are adopted for the *one* and *two* overlapped layered areas.

Secondly, uncertainties on the actual geometry must also be considered if a quantitative comparison between experiments and theoretical prediction is performed. Numerical results reported in Figure 6 are obtained on the geometry rebuilt starting from the SEM images of Figure 3, but uncertainties are present especially on the beams cross-sections. To quantify the effect of geometric imperfections, we compare the bandgap computed on the unit cell with a = 200 µm with the bandgaps obtained on two unit cells obtained by reducing/increasing the beams cross-section of 0.5 µm each side. The same Young's modulus of 2.3 GPa employed before is considered here for the sake of simplicity. The bandgap of the a = 200 µm unit cell covers the frequency range 577 kHz–3.53 MHz, by reducing the beams cross-section of 0.5 µm each side, we obtain a bandgap in the range 539 kHz–3.45 MHz, while increasing the beams cross-section of the same quantity we obtain a 624 kHz–3.70 MHz bandgap. As expected, geometric dimensions are of fundamental importance in the quantitative agreement between experiments and numerical predictions. The bandgap opening frequency can indeed vary in a range of amplitude 85 kHz. A precise reconstruction of the geometry of the fabricated metastructures is indeed required.

Finally, viscous properties of the resin have been neglected in this work for the sake of simplicity. They can influence the attenuation level obtained through the metastructures and also the bandgap opening and closing frequencies. Future work will address such aspects.

6. Conclusions

The main findings of this work can be summarized as follows:

- three prototypes made by a 2 × 2 × 3 periodic repetition of unit cells of 100, 150 and 200 µm width were fabricated through the 2PP technique, numerically simulated in COMSOL Multiphysics and experimentally tested through a Michelson interferometer;
- a good agreement between theoretical predictions based on dispersion analyses of the ideally periodic material, attenuation analyses of the designed metastructures and experimental results on the fabricated metastructures was achieved;

- the influence of the layered structure obtained by 2PP on the elastic properties of the polymerized material was highlighted and simulated.

The possibility to grade the properties and the anisotropy of the resin can allow the design of new micro-structures. As an additional perspective, it is worth mentioning that the range of materials that can be 3D structured by 2PP is rapidly extending, encompassing glass [48], metal [49], and other inorganic compounds [50]. The multiscale fabrication capabilities of 2PP, from few micrometers to millimeters, combined with the use of materials with different stiffnesses, open unexplored possibilities in the development of application-tailored 3D phononic structures operating at different frequency intervals.

Author Contributions: V.Z., conceptualization, software, formal analysis, methodology, writing—original draft preparation; L.P., data curation, investigation, writing—review and editing; T.Z., data curation,writing—review and editing; R.O., project administration, supervision, writing—review and editing; C.C., conceptualization, project administration, supervision, writing—original draft preparation; A.C., conceptualization, supervision, writing—review and editing. All authors have read and agreed to the published version of the manuscript.

Funding: This research received no external funding.

Institutional Review Board Statement: Not applicable.

Informed Consent Statement: Not applicable.

Data Availability Statement: The data that support the findings of this study are available from the corresponding author upon reasonable request.

Acknowledgments: The authors thank Claudio Conci from Politecnico di Milano for providing the SZ2080 photoresist.

Conflicts of Interest: The authors declare no conflict of interest.

Abbreviations

The following abbreviations are used in this manuscript:

2PP	Two-Photon Polymerization
MEMS	Micro Electro Mechanical Systems
IBZ	Irreducible Brillouin Zone

References

1. Corigliano, A.; Ardito, R.; Comi, C.; Frangi, A.; Ghisi, A.; Mariani, S. *Mechanics of Microsystems*; Wiley: Hoboken, NJ, USA, 2018 . ISBN 978-1-119-05383-5
2. Zega, V.; Silva, P.; Geers, M.; Kouznetsova, V. Experimental proof of emergent subharmonic attenuation zones in a nonlinear locally resonant metamaterial. *Sci. Rep.* **2020**, *10*, 12041. [CrossRef] [PubMed]
3. Fronk, M.D.; Leamy, M.J. Internally resonant wave energy exchange in weakly nonlinear lattices and metamaterials. *Phys. Rev. E* **2019**, *100*, 032213. [CrossRef]
4. Jiao, W.; Gonella, S. Intermodal and Subwavelength Energy Trapping in Nonlinear Metamaterial Waveguides. *Phys. Rev. Appl.* **2018**, *10*, 024006. [CrossRef]
5. Jin, Y.; Torrent, D.; Pennec, Y.; Pan, Y.; Djafari-Rouhani, B. Simultaneous control of the S0 and A0 Lamb modes by graded phononic crystal plates. *J. Appl. Phys.* **2015**, *117*, 244904. [CrossRef]
6. Tol, S.; Degertekin, F.L.; Erturk, A. Phononic crystal Luneburg lens for omnidirectional elastic wave focusing and energy harvesting. *Appl. Phys. Lett.* **2017**, *111*, 013503. [CrossRef]
7. Zhao, L.; Lai, C.; Yu, M. Modified structural Luneburg lens for broadband focusing and collimation. *Mech. Syst. Signal Process.* **2020**, *144*, 106868. [CrossRef]
8. Chaplain, G.J.; Craster, R.V. Flat lensing by graded line meta-arrays. *Phys. Rev. B* **2019**, *99*, 220102. [CrossRef]
9. Liu, J.; Guo, H.; Wang, T. A review of acoustic metamaterials and phononic crystals. *Crystals* **2020**, *10*, 305. [CrossRef]
10. Vasileiadis, T.; Varghese, J.; Babacic, V.; Gomis-Bresco, J.; Navarro Urrios, D.; Graczykowski, B. Progress and perspectives on phononic crystals. *J. Appl. Phys.* **2021**, *129*, 160901 . [CrossRef]
11. He, J.; He, X.; Dong, T.; Wang, S.; Fu, M.; Zhang, Y. Recent progress and applications of terahertz metamaterials. *J. Phys. Appl. Phys.* **2021**, *55*, 123002. [CrossRef]

12. Seshia, A.A.; Palaniapan, M.; Roessig, T.A.; Howe, R.T.; Gooch, R.W.; Schimert, T.R.; Montague, S. A vacuum packaged surface micromachined resonant accelerometer. *J. Microelectromech. Syst.* **2002**, *11*, 784–793. [CrossRef]
13. Liewald, J.; Kuhlmann, B.; Balslink, T.; Trächtler, M.; Dienger, M.; Manoli, Y. 100 kHz MEMS Vibratory Gyroscope. *J. Microelectromech. Syst.* **2013**, *22*, 1115–1125. [CrossRef]
14. Agarwal, M.; Park, K.K.; Hopcroft, M.; Chandorkar, S.; Candler, R.N.; Kim, B.; Melamud, R.; Yama, G.; Murmann, B.; Kenny, T.W. Effects of Mechanical Vibrations and Bias Voltage Noise on Phase Noise of MEMS Resonator Based Oscillators. In Proceedings of the 19th IEEE International Conference on Micro Electro Mechanical Systems, Istanbul, Turkey, 22–26 January 2006; pp. 154–157.
15. Yoon, S.W.; Lee, S.; Najafi, K. Vibration-induced errors in MEMS tuning fork gyroscopes. *Sens. Actuators A Phys.* **2012**, *180*, 32–44. [CrossRef]
16. Yoon, S.W.; Lee, S.; Perkins, N.C.; Najafi, K. Analysis and wafer-level design of a high-order silicon vibration isolator for resonating MEMS devices. *J. Micromech. Microeng.* **2010**, *21*, 015017. [CrossRef]
17. Kim, S.J.; Dean, R.; Flowers, G.; Chen, C. Active Vibration Control and Isolation for Micromachined Devices. *J. Mech. Des.* **2009**, *131*, 657–664. [CrossRef]
18. Yao, Z.; Zega, V.; Su, Y.; Zhou, Y.; Ren, J.; Zhang, J.; Corigliano, A. Design, Fabrication and Experimental Validation of a Metaplate for Vibration Isolation in MEMS. *J. Microelectromech. Syst.* **2020**, *29*, 1401–1410. [CrossRef]
19. Lee, H.K.; Melamud, R.; Chandorkar, S.; Salvia, J.; Yoneoka, S.; Kenny, T.W. Stable Operation of MEMS Oscillators Far Above the Critical Vibration Amplitude in the Nonlinear Regime. *J. Microelectromech. Syst.* **2011**, *20*, 1228–1230. [CrossRef]
20. Jaakkola, A.; Prunnila, M.; Pensala, T.; Dekker, J.; Pekko, P. Design Rules for Temperature Compensated Degenerately n-Type-Doped Silicon MEMS Resonators. *J. Microelectromech. Syst.* **2015**, *24*, 1832–1839. [CrossRef]
21. van Beek, J.T.M.; Puers, R. A review of MEMS oscillators for frequency reference and timing applications. *J. Micromech. Microeng.* **2011**, *22*, 013001. [CrossRef]
22. D'Alessandro, L.; Belloni, E.; Ardito, R.; Braghin, F.; Corigliano, A. Mechanical low-frequency filter via modes separation in 3D periodic structures. *Appl. Phys. Lett.* **2017**, *111*, 231902. [CrossRef]
23. D'Alessandro, L.; Zega, V.; Ardito, R.; Corigliano, A. 3D auxetic single material periodic structure with ultra-wide tunable bandgap. *Sci. Rep.* **2018**, *8*, 2262. [CrossRef] [PubMed]
24. Yan, L.; Yang, Y.; James, G.K.; Ankit, S. 3-D phononic crystals with ultra-wide band gaps. *Sci. Rep.* **2017**, *7*, 43407.
25. Li, W.; Meng, F.; Li, Y.; Huang, X. Topological design of 3D phononic crystals for ultra-wide omnidirectional bandgaps. *Struct. Multidisc. Optim.* **2019**, *60*, 2405–2415. [CrossRef]
26. Fang, X.; Wen, J.; Bonello, B.; Yin, J.; Yu, D. Ultra-low and ultra-broad-band nonlinear acoustic metamaterials. *Nat. Commun.* **2017**, *8*, 1288. [CrossRef]
27. Bortot, E.; Amir, O.; Shmuel, G. Topology optimization of dielectric elastomers for wide tunable band gaps. *Int. J. Solids Struct.* **2018**, *143*, 262–273. [CrossRef]
28. Bonnecaze, R.T.; Rodin, G.J.; Sigmund, O.; Søndergaard Jensen, J. Systematic design of phononic bandgap materials and structures by topology optimization. *Philos. Trans. R. Soc. Lond. Ser. A Math. Phys. Eng. Sci.* **2003**, *361*, 1001–1019.
29. Han, X.K.; Zhang, Z. Topological Optimization of Phononic Crystal Thin Plate by a Genetic Algorithm. *Sci. Rep.* **2019**, *9*, 8331. [CrossRef]
30. D'Alessandro, L.; Bahr, B.; Daniel, L.; Weinstein, D.; Ardito, R. BESO approach to topology optimization of GaN phononic crystals. In Proceedings of the VII European Congress on Computational Methods in Applied Sciences and Engineering, Crete, Greece, 5–10 June 2016 ; pp. 3583–3595.
31. Meng, F.; Huang, X.; Jia, B. Bi-directional evolutionary optimization for photonic band gap structures. *J. Comput. Phys.* **2015**, *302*, 393–404. [CrossRef]
32. Sharma, A.; Kosta, M.; Shmuel, G.; Amir, O. Gradient-based topology optimization of soft dielectrics as tunable phononic crystals. *Compos. Struct.* **2022**, *280*, 114846 . [CrossRef]
33. Olsson, R.H.; Ziaei-Moayyed, M.; Kim, B.; Reinke, C.; Su, M.F.; Hopkins, P.; Soliman, Y.M.; Goettler, D.F.; Leseman, Z.C.; El-Kady, I. Micro and nano fabricated phononic crystals: Technology and applications. In Proceedings of the 2011 IEEE International Ultrasonics Symposium, Orlando, FL, USA, 18–21 October 2011; pp. 983–988.
34. Olsson, R.H.; El-Kady, I. Microfabricated phononic crystal devices and applications. *Meas. Sci. Technol.* **2008**, *20*, 012002. [CrossRef]
35. Feng, D.; Jiang, W.; Xu, D.; Xiong, B.; Wang, Y. Micro-silicon phononic crystal with locally resonant theory. *Appl. Phys. Lett.* **2017**, *110*, 171902. [CrossRef]
36. Cang, Y.; Jin, Y.; Djafari-Rouhani, B.; Fytas, G. Fundamentals, progress and perspectives on high-frequency phononic crystals. *J. Phys. Appl. Phys.* **2022**, *55*, 193002. [CrossRef]
37. Maruo, S.; Kawata, S. Two-photon absorbed photopolymerization for three-dimensional microfabrication. In Proceedings of the IEEE The Tenth Annual International Workshop on Micro Electro Mechanical Systems, Nagoya, Japan, 26–30 January 1997; pp. 169–174.
38. Farsari, M.; Vamvakaki, M.; Chichkov, B.N. Multiphoton polymerization of hybrid materials. *J. Opt.* **2010**, *12*, 124001 . [CrossRef]
39. Baldacchini, T. *Three-Dimensional Microfabrication Using Two-Photon Polymerization*; William Andrew: Norwich, NY, USA , 2015.
40. Valdevit, L.; Bauer, J. Fabrication of 3D micro-/nanoarchitected materials. In *Three-Dimensional Microfabrication Using Two-Photon Polymerization*; William Andrew: Norwich, NY, USA, 2019; pp. 541–576.

41. D'Alessandro, L.; Belloni, E.; Ardito, R.; Corigliano, A.; Braghin, F. Modeling and experimental verification of an ultra-wide bandgap in 3D phononic crystal. *Appl. Phys. Lett.* **2016**, *109*, 221907. [CrossRef]
42. Brillouin, L. *Wave Propagation in Periodic Structures*; Dover Publications: Mignola, NY, USA, 1953.
43. Srikantha Phani, A.; Woodhouse, J.; Fleck, N. Wave propagation in two-dimensional periodic lattices. *J. Acoust. Soc. Am.* **2006**, *119*, 1995–2005. [CrossRef]
44. Pertoldi, L.; Zega, V.; Comi, C.; Osellame, R. Dynamic mechanical characterization of two-photon-polymerized SZ2080 photoresist. *J. Appl. Phys.* **2020**, *128*, 175102. [CrossRef]
45. Flamourakis, G.; Spanos, I.; Vangelatos, Z.; Manganas, P.; Papadimitriou, L.; Grigoropoulos, C.; Ranella, A.; Farsari, M. Laser-made 3D Auxetic Metamaterial Scaffolds for Tissue Engineering Applications. *Macromol. Mater. Eng.* **2020**, *305*, 2000238. [CrossRef]
46. Wang, G.; Wen, X.; Wen, J.; Shao, L.; Liu, Y. Two-dimensional locally resonant phononic crystals with binary structures. *Phys. Rev. Lett.* **2004**, *93*, 154302. [CrossRef]
47. Comi, C.; Marigo, J.J. Homogenization Approach and Bloch-Floquet Theory for Band-Gap Prediction in 2D Locally Resonant Metamaterials. *J. Elast.* **2020**, *139*, 61–90 . [CrossRef]
48. Hong, Z.; Ye, P.; Loy, D.A.; Liang, R. Three-dimensional printing of glass micro-optics. *Optica* **2021**, *8*, 904–910. [CrossRef]
49. Ma, Z.C.; Zhang, Y.L.; Han, B.; Chen, Q.D.; Sun, H.B. Femtosecond-Laser Direct Writing of Metallic Micro/Nanostructures: From Fabrication Strategies to Future Applications. *Small Methods* **2018**, *2*, 1700413. [CrossRef]
50. Gonzalez-Hernandez, D.; Varapnickas, S.; Merkininkaitė, G.; Čiburys, A.; Gailevičius, D.; Šakirzanovas, S.; Juodkazis, S.; Malinauskas, M. Laser 3D Printing of Inorganic Free-Form Micro-Optics. *Photonics* **2021**, *8*, 577 . [CrossRef]